J. Fluid Mech. (2006), *vol.* 549, *pp.* 315–341.
doi:10.1017/S0022112005008037 Printed in the United Kingdom

Theoretical model for sound radiation from annular jet pipes: far- and near-field solutions

By G. GABARD[1]† AND R. J. ASTLEY[2]

[1]Laboratoire Roberval de Mécanique, Université de Technologie de Compiègne, 60205 Compiègne, France

[2]Institute of Sound and Vibration Research, University of Southampton, Southampton SO17 1BJ, UK

(Received 31 January 2005 and in revised form 8 August 2005)

An analytical model is presented for sound radiation from a semi-infinite unflanged annular duct. The duct carries a jet which issues into a uniform mean flow while an inner cylindrical centre body extends downstream from the duct exit. This geometrical arrangement forms an idealized representation of a turbofan exhaust where noise propagates along the annular bypass duct, refracts through the external bypass stream and radiates to the far field. The instability wave of the vortex sheet and its interaction with the acoustic field are accounted for in an exact way in the current solution. Efficient numerical procedures are presented for evaluating near-field and far-field solutions, and these are used as the basis for a parametric study to illustrate the effect of varying the hub–tip ratio, and the ratio of jet velocity to external flow velocity. Since the 'Kutta' condition can be turned on and off in the current solution, this capability is used to assess the effect of vortex shedding on noise radiation. Far-field directivity patterns are presented for single modes and also for a multi-mode 'broadband' source model in which all cut-on modes are assumed to be present with equal modal power. Good agreement is found between analytical solutions and experimental data. Near-field pressure maps of the acoustic and instability portions of the solution are generated for selected tones.

1. Introduction

The analytic solution reported in this paper forms a simple model for the radiation of fan noise from the bypass duct of a turbofan aeroengine. It offers an idealized solution for this problem and acts as an exact reference solution against which more comprehensive methods can be assessed. Aft radiated fan noise has become a critical noise source in modern high bypass ratio (HBR) turbofan engines, eclipsing jet mixing as the dominant noise source at high engine power settings. While satisfactory computational schemes exist for predicting forward radiated fan noise, the prediction and treatment of aft fan noise has received less attention and is less well understood. It presents a more challenging task for computational aeroacoustics (CAA) owing to the presence of the shear layer which separates the bypass stream from the free field. The correct treatment of refraction through this layer and of the hydrodynamic instabilities which arise within it present practical problems for which robust numerical solutions have yet to be demonstrated. While the probable future for aft fan noise

† Present address: Institute of Sound and Vibration Research University of Southampton, Southampton SO17 1BJ, UK; gabard@soton.ac.uk

prediction lies in the development of appropriate numerical schemes which can deal accurately not only with the shear layer, but also with non-uniform mean flows and real nacelle geometries, idealized solutions such as the one to be presented here are useful, both as a basis for simple parametric studies and as benchmark solutions for subsequent numerical treatments. The current solution describes the sound field radiated from a semi-infinite axisymmetric circular or annular duct which carries a subsonic jet. In the annular case, a cylindrical centre body extends downstream from the duct exit, forming a simple analogue for the after-body of a turbofan engine. The solution which is presented here, although it applies only to an idealized geometry, contains the essential elements of more realistic configurations.

The first of these is simply wave scattering by the duct lip and the centre body. While analytical solutions for radiation from a flanged circular or annular duct are reasonably straightforward, the problem of an unflanged duct is more difficult since it involves mixed and semi-infinite boundary conditions on the duct wall and in the fluid. Levine & Schwinger (1948) derived an analytical solution for the case of a semi-infinite circular duct in the absence of flow by using the Wiener–Hopf method which provides a systematic approach for this class of problem. The key step in this method is the factorization of the so-called Wiener–Hopf kernel, but in many cases there is no analytical factorization. Explicit expressions can be obtained for the analogous two-dimensional problem (Aublin 1996), but these are not available for the axisymmetric case. Much has been published, however, on various approximations (high or low frequency, small Strouhal number, etc.) and several schemes have been proposed to evaluate the factorization numerically (Ramakrishnan 1982; Rienstra 1984; Cho 1996).

The presence of mean flow in the free stream and in the duct modifies in a subtle way the physics of the problem, even when the flow velocity is the same in the two regions. The convective effect of the mean flow alters the general behaviour of the waves and the singularity at the lip of the duct requires particular attention. For an inlet problem (the fluid flows into the duct) the pressure is singular, but integrable, at the leading edge. For an outlet problem (the fluid flows out of the duct) a vortex sheet exists at the continuation of the duct. This is produced by the shedding of vorticity in the vicinity of the trailing edge, the amount of shed vorticity being given by the Kutta condition. Carrier (1956) was the first to consider this effect for a uniform mean flow. Homicz & Lordi (1975) derived expressions by applying a Lorentz transform to the solution for the no-flow case, applying it to the pressure and velocity potential equations for the exhaust and intake cases, respectively. By comparing the incident and radiated energy, Rienstra (1984) showed that the interaction between the acoustic field and the vortex sheet is complex. Depending on the parameters, the latter can either absorb energy from, or add energy to, the acoustic field. Furthermore, Cargill (1982*a*, *b*) considered the problem for low or high frequencies, whereas Rienstra (1983) studied the limit for small Strouhal numbers.

A further complication arises when the mean flow velocities in the jet and in the surrounding fluid are different. Acoustic waves are then refracted by the velocity discontinuity across the vortex sheet, and the radiated energy is deflected away from the jet to give an acoustic 'cone of silence' in the jet direction. In addition, the velocity discontinuity introduces a convective instability, i.e. the Kelvin–Helmholtz instability of the vortex sheet, which grows exponentially in the streamwise direction. In this situation, particular care should be taken to obtain solutions which satisfy the causality condition. Jones and Morgan have devoted several papers to the stability of vortex sheets and proposed a systematic method for deriving causal solutions (see Jones & Morgan 1972; Jones 1973*a*, *b*, 1975*a*, *b*, 1977; Morgan 1974, 1975).

Crighton & Leppington (1974) and Morgan (1974) have studied the radiation of sound through a vortex sheet emanating from a semi-infinite flat plate and have shown that the plate couples the instability wave with the acoustic field so that it is not possible to remove the instability without modifying the acoustic field. The most general solution to date is that of Munt who considered the problem of a circular jet pipe and studied the effect of various parameters on far-field directivity and reflection coefficients (Munt 1977, 1990).

Taylor, Crighton & Cargill (1993) considered combustion noise radiating from a buried nozzle, i.e. coaxial jet pipes with the outer duct extending beyond the inner duct. The combustion noise was described as a plane wave originating from the inner pipe, and vortex shedding was modelled by the presence of vortex sheets separating the inner, outer and ambient flows. Taylor *et al.* (1993) derived an asymptotic solution in the low-frequency limit by assuming that the nozzle lips only interact through travelling plane waves.

All of the references cited above describe theoretical studies. Several experimental investigations have also been carried out, see, for instance, Alfredson & Davies (1970), Plumblee & Dean (1973), Schlinker (1977), Bhattacharya (1980) and Bento Coelho (1980).

An important aspect addressed in the present work, but not dealt with in previous studies, is the effect of a centre body extending beyond the jet pipe. This is important in turbofan bypass applications where the after-body may have a significant effect on the noise radiated from the bypass duct. By using the Wiener–Hopf technique, Rienstra (1984) derived the general solution for a semi-infinite duct with an infinite centre body for the case of uniform flow across the jet and bypass stream. This solution is extended in the current article to include a bypass shear layer. Alternatively, the current solution can be regarded as an extension of the solution of Munt (1977) which includes a shear layer, but not a centre body.

The first aim of the present work is simply to derive an exact solution which includes both variable jet and free-stream velocities and a centre body. The Wiener–Hopf approach is used, building on the work of both Munt (1977) and Rienstra (1984).

The second aim of this paper is to formulate robust and efficient numerical procedures for evaluating the above solution so that it can be implemented at realistic frequencies and Mach numbers to obtain estimates of radiated sound power for practical turbofan operating conditions. These generally involve quite high frequencies (ka values in the range 0–60 for a modern HBR engine) and subsonic Mach numbers in the range 0–0.8 at the duct exit.

The layout of this paper is as follows. The hypotheses and basic equations of the problem are set out in § 2. In § 3, the Wiener–Hopf method is used to derive the general solution for the diffracted acoustic field together with the far-field approximation and the reflection coefficients at the duct termination. Results are presented in § 4. The general analysis is presented for the case of annular duct with a centre body. The particular case of a hollow duct is treated where necessary as a special case. The practical implementation and numerical evaluation of the solution is described in Appendix A.

2. Description of the problem

Consider a cylindrical duct with annular cross-section (see figure 1). The outer wall of the duct is semi-infinite ($z < 0$) of radius R_0 and zero thickness. The centre body is infinite in the axial direction and of radius R_1. Both surfaces of the duct, inner and outer, are rigid and impervious. The duct contains a uniform axial mean flow of

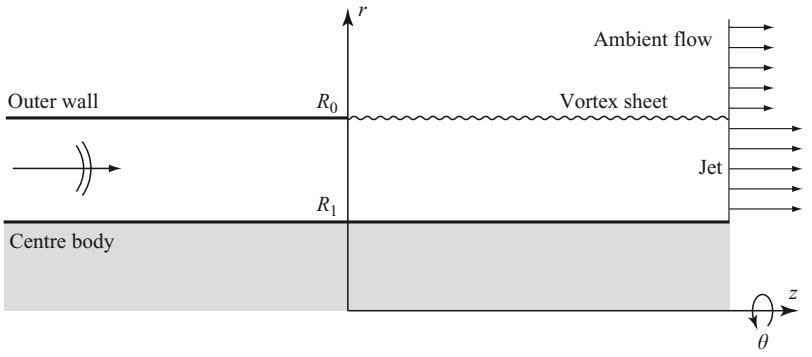

FIGURE 1. A sketch of the annular duct.

density ρ_j, velocity v_j and speed of sound c_j. In the outer region $r > R_0$, the ambient flow is axial and uniform of density ρ_0, velocity v_0 and speed of sound c_0. The jet emanating from the duct exit is separated from the ambient flow by a vortex sheet ($z > 0$ and $r = R_0$). In what follows, the mean flow is said to be non-uniform when the jet properties (ρ_j, c_j, v_j) differ from that of the ambient flow (ρ_0, c_0, v_0) although the flow profile is constant in each region.

All of the variables of the problem are made dimensionless by using the outer duct radius R_0 and the ambient flow properties ρ_0 and c_0 as reference values. Both in the jet and the ambient flow, the disturbances are considered to be linear and purely acoustic (i.e. irrotational). Except at the vortex sheet, the jet and ambient flow do not carry hydrodynamic disturbances. The acoustic solution is therefore described by a velocity potential ϕ which satisfies convected wave equations in the jet and the ambient flow: i.e.

$$\left(\frac{\partial}{\partial t} + M_0\frac{\partial}{\partial z}\right)^2 \phi - \Delta\phi = 0, \quad r > 1, \tag{2.1}$$

$$C_1^2\left(\frac{\partial}{\partial t} + M_1\frac{\partial}{\partial z}\right)^2 \phi - \Delta\phi = 0, \quad h < r < 1, \tag{2.2}$$

where $M_0 = v_0/c_0$ and $M_1 = v_j/c_0$ are Mach numbers of the ambient flow and the jet, respectively (note however that M_1 is not the local Mach number since it is defined in terms of the sound speed in the free stream). The ratio of the sound speeds and the hub–tip ratio (i.e. the ratio of the inner to outer duct radius) are denoted $C_1 = c_0/c_j$, and $h = R_1/R_0$, respectively.

The acoustic pressure p, velocity $\boldsymbol{v}$ and density ρ are given by:

$$p = -\left(\frac{\partial\phi}{\partial t} + M_0\frac{\partial\phi}{\partial z}\right), \quad \boldsymbol{v} = \nabla\phi, \quad \rho = p, \quad r > 1, \tag{2.3}$$

$$p = -D_1\left(\frac{\partial\phi}{\partial t} + M_1\frac{\partial\phi}{\partial z}\right), \quad \boldsymbol{v} = \nabla\phi, \quad \rho = pC_1^2, \quad h < r < 1, \tag{2.4}$$

where $D_1 = \rho_j/\rho_0$ is the ratio of the jet and ambient densities. The duct walls are rigid so we have:

$$\frac{\partial\phi}{\partial r}(h, \theta, z) = 0, \quad \forall z, \quad \frac{\partial\phi}{\partial r}(1^-, \theta, z) = \frac{\partial\phi}{\partial r}(1^+, \theta, z) = 0, \quad z \leqslant 0. \tag{2.5}$$

The interactions of the acoustic fields on both sides of the vortex layer are described by two continuity conditions. The kinematic condition states that the normal particle

displacement w is continuous across the vortex sheet. Since the normal acoustic velocity is the material derivative of the normal particle displacement, the velocity potential ϕ is related to w by

$$\left(\frac{\partial}{\partial t}+M_0\frac{\partial}{\partial z}\right)w(\theta,z)=\frac{\partial\phi}{\partial r}(1^+,\theta,z),\quad z>0, \tag{2.6}$$

$$\left(\frac{\partial}{\partial t}+M_1\frac{\partial}{\partial z}\right)w(\theta,z)=\frac{\partial\phi}{\partial r}(1^-,\theta,z),\quad z>0. \tag{2.7}$$

For an inviscid fluid, the dynamic condition implies that the pressure is continuous across the vortex sheet: $p(1^+,\theta,z)=p(1^-,\theta,z)$. By using equations (2.3)–(2.4), this condition is written in terms of the velocity potential:

$$\left(\frac{\partial}{\partial t}+M_0\frac{\partial}{\partial z}\right)\phi(1^+,\theta,z,t)=D_1\left(\frac{\partial}{\partial t}+M_1\frac{\partial}{\partial z}\right)\phi(1^-,\theta,z,t),\quad z>0. \tag{2.8}$$

2.1. *Incident wave*

Now consider time-harmonic problems, with a $\exp(-\mathrm{i}\omega t)$ dependence. Inside the duct, the acoustic field can be described as a sum of left- and right-propagating eigenmodes:

$$\phi(r,z,\theta,t)=\sum_{m=-\infty}^{+\infty}\sum_{n=0}^{+\infty}[B^-_{mn}\exp(\mathrm{i}\omega\mu^-_{mn}z) + B^+_{mn}\exp(\mathrm{i}\omega\mu^+_{mn}z)]\Psi_{mn}(r)\exp(\mathrm{i}m\theta-\mathrm{i}\omega t), \tag{2.9}$$

where m and n are the circumferential and radial mode orders. The mode shapes are given by $\Psi_{mn}(r)=\mathrm{Y}'_m(\alpha_{mn}h)\mathrm{J}_m(\alpha_{mn}r)-\mathrm{J}'_m(\alpha_{mn}h)\mathrm{Y}_m(\alpha_{mn}r)$. The radial wavenumbers α_{mn} are solutions of the characteristic equation:

$$\Lambda(z)=\mathrm{Y}'_m(zh)\mathrm{J}'_m(z)-\mathrm{J}'_m(zh)\mathrm{Y}'_m(z)=0, \tag{2.10}$$

and the axial wavenumber $\mu^\pm_{mn}$ is related to α_{mn} through the dispersion relation in the duct:

$$\mu^\pm_{mn}=\frac{\pm\sqrt{C_1^2-(1-M_1^2C_1^2)\alpha^2_{mn}/\omega^2}-M_1C_1^2}{1-M_1^2C_1^2}.$$

For the plane waves, we have simply $\Psi_{00}=1$ and $\mu^\pm_{00}=C_1/(M_1C_1\pm1)$.

Since any sound field in the duct is a sum of eigenmodes, we are primarily interested in the radiated noise produced by a single eigenmode (m,n) propagating in the duct towards the exit plane and then radiating in the free field. This incident wave is taken to be

$$\phi_0(r,\theta,z,t)=\begin{cases}0, & r>1,\\ \Psi_{mn}(r)\exp(\mathrm{i}\omega\mu^+_{mn}z+\mathrm{i}m\theta-\mathrm{i}\omega t), & h<r<1.\end{cases} \tag{2.11}$$

This incident wave ϕ_0 satisfies the convected wave equation (2.2) in the jet and the hard-wall boundary conditions in the duct. Then, we write the acoustic field as the sum of the incident wave ψ_0 and a diffracted field ψ. Since the geometry and boundary conditions are axisymmetric, the diffracted field retains the same azimuthal and time dependencies as the incident wave:

$$\phi(r,\theta,z,t)=[\psi(r,z)+\psi_0(r,z)]\exp(\mathrm{i}m\theta-\mathrm{i}\omega t),\quad \psi_0(r,z)=\Psi_{mn}(r)\exp(\mathrm{i}\omega\mu^+_{mn}z).$$

Accordingly, the radial displacement of the vortex sheet is written $w(\theta,z,t)=\xi(z)\exp(\mathrm{i}m\theta-\mathrm{i}\omega t)$. In what follows, the harmonic dependence $\exp(\mathrm{i}m\theta-\mathrm{i}\omega t)$ will be

omitted and the variables p, ρ and $\boldsymbol{v}$ will refer to the diffracted part of the acoustic field. The complex amplitude of the diffracted field ψ is the solution of the following set of equations:

$$\frac{1}{r}\frac{\partial}{\partial r}\left(r\frac{\partial \psi}{\partial r}\right)+\frac{\partial^2\psi}{\partial z^2}-\frac{m^2}{r^2}\psi-\left(-\mathrm{i}\omega+M_0\frac{\partial}{\partial z}\right)^2\psi=0,\quad r>1, \tag{2.12}$$

$$\frac{1}{r}\frac{\partial}{\partial r}\left(r\frac{\partial \psi}{\partial r}\right)+\frac{\partial^2\psi}{\partial z^2}-\frac{m^2}{r^2}\psi-C_1^2\left(-\mathrm{i}\omega+M_1\frac{\partial}{\partial z}\right)^2\psi=0,\quad h<r<1 \tag{2.13}$$

$$\frac{\partial \psi}{\partial r}(h,z)=0,\quad \forall z, \tag{2.14a}$$

$$\frac{\partial \psi}{\partial r}(1^-,z)=\frac{\partial \psi}{\partial r}(1^+,z)=0,\quad z\leqslant 0, \tag{2.14b}$$

$$\left(-\mathrm{i}\omega+M_0\frac{\partial}{\partial z}\right)\xi(z)=\frac{\partial \psi}{\partial r}(1^+,z),\quad z>0, \tag{2.15}$$

$$\left(-\mathrm{i}\omega+M_1\frac{\partial}{\partial z}\right)\xi(z)=\frac{\partial \psi}{\partial r}(1^-,z),\quad z>0, \tag{2.16}$$

$$\left(-\mathrm{i}\omega+M_0\frac{\partial}{\partial z}\right)\psi(1^+,z)=D_1\left(-\mathrm{i}\omega+M_1\frac{\partial}{\partial z}\right)[\psi(1^-,z)+\psi_0(1^-,z)],\quad z>0. \tag{2.17}$$

2.2. *Edge conditions*

A key aspect of the present problem is to describe correctly the behaviour of the solution at the lip of the duct ($z=0$, $r=1$) since the acoustic field can be singular at that point. A first requirement is that the overall force applied by the fluid on any segment of the duct walls is finite. This means that the pressure near the lip is integrable and, consequently, that the velocity potential is finite around the lip. Yet, this requirement is not sufficient to define a unique solution to the problem. The additional information required to uniquely define the solution is the amount of vorticity shed from the lip.

When written in terms of the velocity potential, the part of the solution which describes vortex shedding is discontinuous across the vortex sheet (in fact, ϕ and $\partial\phi/\partial z$ are discontinuous, but $\partial\phi/\partial r$ is continuous). If no vorticity is shed from the lip, the velocity potential and its derivatives are continuous. It can then be shown that $\phi(1,z)=O(z^{1/2})$ as $z\to 0^+$ which implies that the pressure is singular at the lip. This assumption obviously applies when the lip is a leading edge (that is, for M_0, $M_1<0$) since in that case vorticity shedding is not possible.

On the other hand, we can require that all of the available vorticity is shed from the lip. This is described by the full Kutta condition which states that the pressure is finite at the lip. In that case, the velocity is finite and $\phi(1,z)=O(z^{3/2})$ as $z\to 0^+$ which implies that the pressure is also finite. This condition is generally used for the case of a trailing edge (that is, for M_0, $M_1>0$). However, we must keep in mind that, in practice, the situation lies somewhere between these two extremes since only a part of the vorticity is shed from a trailing edge.

2.3. *Radiation conditions*

The definition of a unique solution also requires that an appropriate radiation condition is prescribed at infinity to ensure that diffracted waves are radiated away

from the open end of the duct (i.e. no energy propagates inwards across a far-field boundary). To ensure that this is the case, we must consider a more general statement of causality which applies for initial-condition problems, of which the Sommerfeld condition is a consequence.

Jones and Morgan have discussed the proper way to obtain time-harmonic solutions which satisfy the causality condition when instability waves are present (see Jones & Morgan 1972; Jones 1973*a*, *b*, 1975*a*, *b*, 1977; Morgan 1974, 1975). The mathematical analysis is carried out using a complex frequency with a positive imaginary part, that is $\omega = \omega_r + \mathrm{i}\omega_i = |\omega|\mathrm{e}^{\mathrm{i}\epsilon}$, $0 \leqslant \epsilon \leqslant \pi/2$. With ω_i sufficiently large, or ϵ close to $\pi/2$, all waves decay exponentially at infinity, including the instability wave, and it can be shown that the solution satisfies the causality condition. The solution with a real frequency is then obtained by taking the limit as $\epsilon \to 0$ and by analytic continuation. More details of this procedure will be given in § 3.3.3, but at this stage, it is only necessary to consider ϵ close to $\pi/2$.

3. Wiener–Hopf method

The Wiener–Hopf method is designed to solve problems with mixed and semi-infinite boundary conditions. For the problem at hand, these are the hard-wall condition on the outer duct for $z < 0$ and the continuity conditions (2.15)–(2.17) for $z > 0$. We follow here the approach of Jones as presented in Noble's book (Noble 1958). An introduction to the Wiener–Hopf method can also be found in Crighton *et al.* (1992).

3.1. *Fourier transforms*

We define the half-range Fourier transforms in the axial direction of the velocity potential ψ:

$$\beta_-(r,u) = \int_{-\infty}^{0} \psi(r,z)\exp(-\mathrm{i}\omega u z)\,\mathrm{d}z, \quad \beta_+(r,u) = \int_{0}^{+\infty} \psi(r,z)\exp(-\mathrm{i}\omega u z)\,\mathrm{d}z,$$

where ωu is the axial wavenumber. The conventional Fourier transform is denoted $\beta = \beta_- + \beta_+$. The use of this transform to the convected wave equations (2.12)–(2.13) yields two Bessel equations:

$$\frac{1}{r}\frac{\partial}{\partial r}\left(r\frac{\partial \beta}{\partial r}\right) + \left(\omega^2\lambda_0^2 - \frac{m^2}{r^2}\right)\beta = 0, \quad r > 1, \tag{3.1}$$

$$\frac{1}{r}\frac{\partial}{\partial r}\left(r\frac{\partial \beta}{\partial r}\right) + \left(\omega^2\lambda_1^2 - \frac{m^2}{r^2}\right)\beta = 0, \quad h < r < 1, \tag{3.2}$$

where we have introduced the radial wavenumbers λ_0 and λ_1 which satisfy the dispersion relations in the ambient flow and the jet, respectively:

$$\lambda_0^2 = (1 - uM_0)^2 - u^2, \quad \lambda_1^2 = C_1^2(1 - uM_1)^2 - u^2. \tag{3.3}$$

The radial wavenumbers are written $\lambda_0 = \lambda_0^-\lambda_0^+$ and $\lambda_1 = \lambda_1^-\lambda_1^+$ with $\lambda_0^\pm = [1 - u(M_0 \pm 1)]^{1/2}$ and $\lambda_1^\pm = [C_1 - u(M_1C_1 \pm 1)]^{1/2}$. The principal branches of the square roots are used so that the branch cuts of $\lambda_0^\pm$ go from $u_0^\pm$ to $\pm\infty$ and the branch cuts of $\lambda_1^\pm$ go from $u_1^\pm$ to $\pm\infty$ where we have defined $u_0^\pm = 1/(M_0 \pm 1)$ and $u_1^\pm = C_1/(M_1C_1 \pm 1)$.

The Fourier transform of the hard-wall boundary condition (2.14*a*) on the centre body is simply $\partial\beta/\partial r(h,u) = 0$. To satisfy this boundary condition, we choose to write

the solution of the Bessel equations (3.1)–(3.2) as follows:

$$\beta(r,u)=\begin{cases}A(u)\mathrm{H}_m^{(1)}(\lambda_0\omega r), & r>1,\\ B(u)[\mathrm{Y}_m'(\lambda_1\omega h)\mathrm{J}_m(\lambda_1\omega r)-\mathrm{J}_m'(\lambda_1\omega h)\mathrm{Y}_m(\lambda_1\omega r)], & h<r<1.\end{cases}\tag{3.4}$$

where J_m and Y_m are the Bessel and Neumann functions of order m, and $\mathrm{H}_m^{(1)}=\mathrm{J}_m+\mathrm{i}\mathrm{Y}_m$ is the Hankel function of the first type. The prime denotes the derivative with respect to the argument.

It is important to describe the regularity of the transform β. To that end, we require that the diffracted field behaves like axial plane waves when $z\to\pm\infty$. It is then straightforward to show that, in the ambient flow $r>1$ the transforms β_- and β_+ are regular in the half-planes R_0^- and R_0^+, respectively, and in the jet $h<r<1$, β_- and β_+ are regular in the half planes R_1^- and R_1^+. The half planes $R_{0,1}^{\pm}$ are defined as follows:

$$\begin{aligned}R_0^{\pm}\ &:\quad \pm\mathrm{Im}(u-u_0^{\pm})<\mp\tan(\epsilon)\mathrm{Re}(u-u_0^{\pm}),\\ R_1^{\pm}\ &:\quad \pm\mathrm{Im}(u-u_1^{\pm})<\mp\tan(\epsilon)\mathrm{Re}(u-u_1^{\pm}).\end{aligned}$$

For all values of r, the transform β is regular in a strip S defined as the intersection of the four half-planes $R_{0,1}^{\pm}$. It is important to note that the imaginary parts of $\lambda_0\omega$ and $\lambda_1\omega$ are positive in S. And therefore, in (3.4), β decreases as $r\to+\infty$.

Furthermore, we introduce the following transforms

$$F_+(u)=\int_0^{+\infty}\xi(z)\exp(-\mathrm{i}\omega uz)\,\mathrm{d}z,\tag{3.5}$$

$$G(u)=\int_{-\infty}^{+\infty}\left[\left(-\mathrm{i}\omega+M_0\frac{\partial}{\partial z}\right)\psi(1^+,z)-D_1\left(-\mathrm{i}\omega+M_1\frac{\partial}{\partial z}\right)\psi(1^-,z)\right]\exp(-\mathrm{i}\omega uz)\,\mathrm{d}z,\tag{3.6}$$

where F_+ represents the Fourier transform of the vortex sheet displacement ξ, and is regular in R_+. G is the Fourier transform of the pressure jump across the outer duct wall (for $z<0$) and the vortex sheet (for $z>0$). The Fourier transforms of equations (2.15), (2.16) and (2.14) give

$$-\mathrm{i}(1-uM_0)F_+(u)=A(u)\lambda_0\mathrm{H}_m^{(1)\prime}(\lambda_0\omega),\tag{3.7}$$

$$-\mathrm{i}(1-uM_1)F_+(u)=B(u)\lambda_1[\mathrm{Y}_m'(\lambda_1\omega h)\mathrm{J}_m'(\lambda_1\omega)-\mathrm{J}_m'(\lambda_1\omega h)\mathrm{Y}_m'(\lambda_1\omega)].\tag{3.8}$$

And, by making use of (3.4), we obtain:

$$\begin{aligned}G(u)=-\mathrm{i}\omega\big\{&(1-uM_0)A(u)\mathrm{H}_m^{(1)}(\lambda_0\omega)\\ &-D_1(1-uM_1)B(u)[\mathrm{Y}_m'(\lambda_1\omega h)\mathrm{J}_m(\lambda_1\omega)-\mathrm{J}_m'(\lambda_1\omega h)\mathrm{Y}_m(\lambda_1\omega)]\big\}.\end{aligned}\tag{3.9}$$

An expression can also be obtained for the half-range transform G_+ by using the continuity of the pressure across the vortex sheet (2.17):

$$G_+(u)=D_1\Psi_{mn}(1)\frac{1-\mu_{mn}^+M_1}{\mu_{mn}^+-u}.\tag{3.10}$$

Then, by combining equations (3.7), (3.8) and (3.9) to eliminate A and B, we derive

the Wiener–Hopf equation:

$$G(u) = G_-(u) + G_+(u) = \omega \frac{K(u)F_+(u)}{\lambda_0 \lambda_1}, \tag{3.11}$$

where K is the Wiener–Hopf kernel:

$$K(u) = D_1(1 - uM_1)^2 \lambda_0 \frac{\mathrm{Y}'_m(\lambda_1 \omega h)\mathrm{J}_m(\lambda_1 \omega) - \mathrm{J}'_m(\lambda_1 \omega h)\mathrm{Y}_m(\lambda_1 \omega)}{\mathrm{Y}'_m(\lambda_1 \omega h)\mathrm{J}'_m(\lambda_1 \omega) - \mathrm{J}'_m(\lambda_1 \omega h)\mathrm{Y}'_m(\lambda_1 \omega)} - (1 - uM_0)^2 \lambda_1 \frac{\mathrm{H}^{(1)}_m(\lambda_0 \omega)}{\mathrm{H}^{(1)\prime}_m(\lambda_0 \omega)}. \tag{3.12}$$

3.2. *Properties of the kernel*

The Wiener–Hopf kernel gathers most of the information concerning the problem at hand and it is worth describing its properties and especially the locations of its poles and zeros.

A first group of zeros and poles is located close to the line crossing the real axis at $u_c = (u_1^+ + u_1^-)/2 = M_1 C_1^2/(M_1^2 C_1^2 - 1)$ at an angle $\pi/2 - \epsilon$. The poles are found when the denominator of the first term in K is zero, that is when $\Lambda(\lambda_1) = 0$ which is precisely the characteristic equation of the infinite annular duct. Therefore, the poles of K correspond to the acoustic modes of the duct.

Secondly, a group of zeros is more related with the behaviour of the vortex sheet. Using high-frequency approximations, analytical expressions can be derived for the location of these zeros (for detailed derivations see Munt 1977). The expressions given by Munt are complicated, and it turns out to be easier, and physically meaningful, to consider the phase speed $\eta = u^{-1}$. With no speed of sound or density mismatch, that is with $C_1 = D_1 = 1$, we have to consider two zeros u_0 and u_1 defined by

$$\eta_{0,1} = \frac{M_0 + M_1}{2} \pm \frac{\mathrm{i}}{2}[1 - (\sqrt{1 + (M_1 - M_0)^2} - 2)^2]^{1/2}. \tag{3.13}$$

For subsonic flows, the second term is always imaginary. Thus, the waves corresponding to these zeros are moving at the average speed of the two streams (the jet and ambient flow) while their exponential growth is controlled by the difference of velocity between the two streams. For a uniform flow, $M_0 = M_1$, $u_0 = u_1 = M_0^{-1}$ is a double zero and satisfies the condition $\mathrm{Im}(\lambda_1) > 0$. However, if $M_0 \neq M_1$, u_1 does not satisfy this condition and only u_0 is a genuine zero of the kernel. In the latter case, u_0 is located in the lower half of the complex plane and represents the instability wave of the shear layer which is growing exponentially in the positive z-direction.

With differentiated density or speed of sound, that is for $D_1 \neq 1$ or $C_1 \neq 1$, additional zeros may be present on the real axis but will not be described here (see Munt 1977).

Another useful piece of information about the Wiener–Hopf kernel is its behaviour for large argument, that is for $|u| \to \infty$. In the strip S, λ_1 has a positive imaginary part so we can use the approximation $K(u) \simeq D_1(1 - uM_1)^2 \lambda_0 + (1 - uM_0)^2 \lambda_1$ and it is clear that $K(u) \sim O(u^3)$ as $|u| \to \infty$ in the strip S. However, in the particular case of no flow, $M_0 = M_1 = 0$, we have $K(u) = O(u)$.

3.3. *General solutions*

The first step for solving the Wiener–Hopf equation (3.11) is to factor the kernel $K(u) = K_+(u)/K_-(u)$ where the split functions $K_\pm$ are regular and non-zero in $R_\pm$. To understand the nature of the factorization of the kernel, we can consider the example of an infinite straight duct. The axial wavenumbers of the eigenmodes, both for

left- and right-running modes, correspond to zeros or poles of the corresponding Wiener–Hopf kernel (in this respect, K is similar to the dispersion relation and the characteristic equation of the problem at hand). Seeking a factorization $K(u) = K_+(u)/K_-(u)$ where $K_\pm$ have no pole or zero in $R_\pm$ is equivalent to factoring the dispersion relation as a product of two distinct dispersion relations so that the left-running modes are solutions of one dispersion relation and the right-running modes are solutions of the other. It is necessary to separate left-from right-running waves because the boundary conditions are different in the negative and positive z-directions.

As explained in the previous section, with a uniform flow, there is a double zero u_0 corresponding to the vorticity shedding whereas, with a non-uniform flow, u_0 is a simple zero describing the instability wave. So, it is convenient to factor explicitly the zero at u_0:

$$K(u) = \frac{\tilde{K}_+(u)}{\tilde{K}_-(u)}(u-u_0)^b, \tag{3.14}$$

where $\tilde{K}_\pm$ are regular and non-zero in $R_\pm$. The exponent b is taken to be 2 for a uniform flow and 1 otherwise. The radial wavenumbers λ_0 and λ_1 are jointly factored using $\lambda_0^\pm$ and $\lambda_1^\pm$. Thus, we obtain:

$$\omega\frac{F_+(u)\tilde{K}_+(u)(u-u_0)^b}{\lambda_0^+(u)\lambda_1^+(u)} = \lambda_0^-\lambda_1^-\tilde{K}_-(u)G_-(u) + \lambda_0^-\lambda_1^-\tilde{K}_-(u)G_+(u).$$

By definition, $\lambda_{0,1}^+$ and $\lambda_{0,1}^-$ are regular and non-zero in R_+ and R_-, respectively. Hence, the left-hand side is regular in R_+. Furthermore, since G_- is regular in R_-, the first term on the right-hand side is also regular in R_-. However, the second term is not regular in R_- since G_+ as a simple pole at $u = \mu_{mn}^+$ and we have to write:

$$\begin{aligned}&\omega\frac{F_+(u)\tilde{K}_+(u)(u-u_0)^b}{\lambda_0^+(u)\lambda_1^+(u)} + \lambda_0^-(\mu_{mn}^+)\lambda_1^-(\mu_{mn}^+)\tilde{K}_-(\mu_{mn}^+)G_+(u)\\ &= G_+(u)[\lambda_0^-(u)\lambda_1^-(u)\tilde{K}_-(u) - \lambda_0^-(\mu_{mn}^+)\lambda_1^-(\mu_{mn}^+)\tilde{K}_-(\mu_{mn}^+)] + \lambda_0^-(u)\lambda_1^-(u)\tilde{K}_-(u)G_-(u),\end{aligned} \tag{3.15}$$

where the left- and right-hand sides are now regular functions in R_+ and R_-, respectively. This identity is satisfied in the strip S. Therefore, by analytic continuation, equation (3.15) defines a single function $E(u)$ regular on the whole complex u-plane.

Then, we must study the behaviour of E as $|u| \to \infty$. First, note that $G_+(u) = O(u^{-1})$ and $\lambda_{0,1}^\pm(u) = O(u^{1/2})$ as $|u| \to \infty$ in S. At this stage, three different cases should be considered.

For an inlet problem, we restrict ourselves to a uniform flow since a non-uniform mean flow is rather unphysical in this case. We have $M_1 = M_0 < 0$ and u_0 is a double zero. Thus, we set $b = 2$ in (3.14) and, using $K(u) = O(u^3)$ as $|u| \to \infty$ in S, it can be shown that the split functions $\tilde{K}_\pm(u)$ behave like $u^{\pm 1/2}$ when $|u| \to \infty$ (Noble 1958, p. 42). The edge of the duct is a leading edge and the corresponding condition is $\psi(1, z) = O(z^{1/2})$ as $z \to 0^+$. With equations (2.3), (3.7) and (3.11), this condition translates into $F_+(u) = O(u^{-3/2})$ and $G_-(u) = O(u^{-1/2})$ as $|u| \to \infty$ in S. It is then straightforward to show that $E(u) = O(1)$ as $|u| \to \infty$ and, by using the extended form of Liouville's theorem (Noble 1958, p. 6), E is a constant and $E = E(u_0) = \lambda_0^-(\mu_{mn}^+)\lambda_1^-(\mu_{mn}^+)\tilde{K}_-(\mu_{mn}^+)G_+(u_0)$. Therefore, we obtain the following expression for F_+:

$$F_+(u) = \frac{\lambda_0^-(\mu_{mn}^+)\lambda_1^-(\mu_{mn}^+)\tilde{K}_-(\mu_{mn}^+)\lambda_0^+(u)\lambda_1^+(u)}{\omega(u-u_0)^b\tilde{K}_+(u)}[G_+(u_0) - G_+(u)]. \tag{3.16}$$

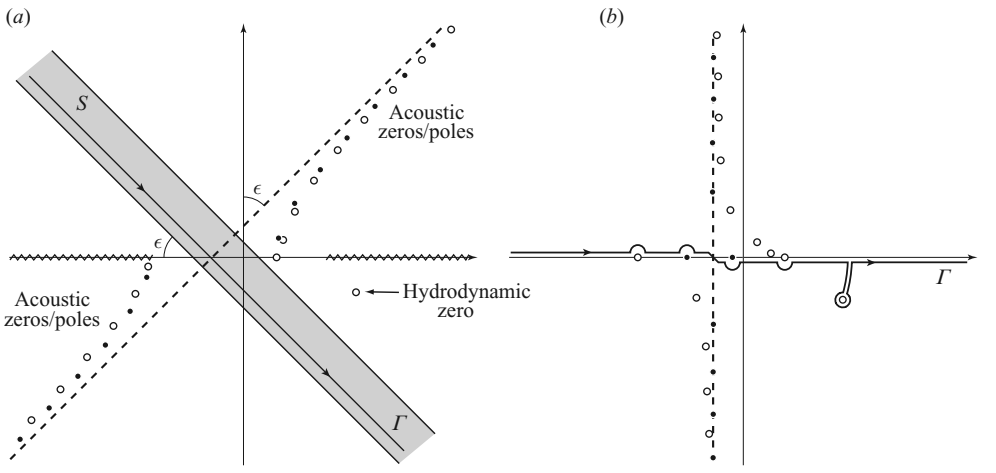

FIGURE 2. Path of integration Γ and locations of $\circ$, the zeros and $\bullet$, poles the of the Wiener–Hopf kernel. The acoustic poles and zeros are close to the dashed line defined by $\arg(u-u_c)=\pi/2-\epsilon$. Parameters are $\omega=4$, $M_1=0.5$, $M_0=0.25$, $D_1=C_1=1$, $h=0$. (*a*) With $\epsilon=\pi/4$, the shaded area is the analytic strip S. (*b*) With $\epsilon\to 0$. Note the indentation of Γ around the acoustic zeros and poles and also around the hydrodynamic zero.

For an outlet problem, we first consider a uniform flow. The edge of the duct is now a trailing edge and the Kutta condition applies: $\psi(1,z)=O(z^{3/2})$ as $z\to 0^+$ which translates into $F_+(u)=O(u^{-5/2})$ and $G_-(u)=O(u^{-1})$ as $|u|\to\infty$ in S. This yields $E(u)=O(u^{-1})$ and, with Liouville's theorem, we have $E(u)\equiv 0$. Secondly, with a non-uniform flow, u_0 is a simple zero and $b=1$. In that case, it can be shown that $\tilde{K}_\pm$ behave like $u^{\pm 1}$ and $E(u)=O(u^{-1/2})$ as $|u|\to\infty$ in S, which implies that E is also identically zero. So for an outlet problem, we obtain

$$F_+(u)=-\frac{\lambda_0^-(\mu_{mn}^+)\lambda_1^-(\mu_{mn}^+)\tilde{K}_-(\mu_{mn}^+)\lambda_0^+(u)\lambda_1^+(u)}{\omega(u-u_0)^b\tilde{K}_+(u)}G_+(u). \tag{3.17}$$

A general expression can be obtained by combining expressions for the inlet and outlet problems. Following Rienstra (1984), we introduce a complex parameter γ to describe the amount of shed vorticity:

$$F_+(u)=\Psi_{mn}(1)D_1(1-\mu_{mn}^+M_1)\frac{\lambda_0^-(\mu_{mn}^+)\lambda_1^-(\mu_{mn}^+)\lambda_0^+(u)\lambda_1^+(u)}{\omega(u-u_0)^b(\mu_{mn}^+-u_0)}\frac{\tilde{K}_-(\mu_{mn}^+)}{\tilde{K}_+(u)}\left(\frac{u-u_0}{u-\mu_{mn}^+}-\gamma\right). \tag{3.18}$$

The amplitude of γ should remain between 0 and 1. With $\gamma=0$, there is no vortex shedding and we obtain (3.16). However, in the case $\gamma=1$, the solution (3.17) with the full Kutta condition is obtained and all the available vorticity is shed from the duct wall. For an inlet problem, γ is necessarily zero since no vortex shedding is possible. However, for an outlet problem it may be interesting to consider $0<|\gamma|<1$ which represents intermediate situations where a limited part of vorticity is shed.

The transform β is readily obtained by making use of equations (3.4), (3.7) and (3.8). The diffracted field is then a solution of an inverse Fourier transform where the path of integration Γ is a line from $-\infty e^{-i\epsilon}$ to $\infty e^{-i\epsilon}$ in the strip S (see figure 2):

$$\psi(r,z)=\frac{\omega}{2\pi}\int_\Gamma \beta(r,u)\exp(i\omega uz)\,du. \tag{3.19}$$

The last step in the derivation is to take the limit $\epsilon \to 0$ and to deform the path of integration by analytic continuation. For ϵ close to $\pi/2$, the path of integration is well away from the poles and zeros of the kernel. However, as ϵ decreases, the zero of the instability wave should cross Γ; but this would violate the analytic continuity so the path of integration is deformed around the zero u_0. Thus the instability wave is included in the solution and it can be shown that the solution is consistent with the causality condition. As shown in figure 2, the path of integration Γ for real-valued frequency ω goes from $-\infty + 0\mathrm{i}$ to $+\infty - 0\mathrm{i}$, crosses the real axis at $u_c = M_1 C_1^2/(M_1^2 C_1^2 - 1)$ and is indented to include the instability wave. Therefore, the general solution for the scattered acoustic field is

$$\psi(r,z) = \frac{\omega}{2\mathrm{i}\pi}\int_\Gamma \frac{(1-uM_0)F_+(u)}{\lambda_0} T_0(r,u)\exp(\mathrm{i}\omega u z)\,\mathrm{d}u, \quad r>1, \tag{3.20}$$

$$\psi(r,z) = \frac{\omega}{2\mathrm{i}\pi}\int_\Gamma \frac{(1-uM_1)F_+(u)}{\lambda_1} T_1(r,u)\exp(\mathrm{i}\omega u z)\,\mathrm{d}u, \quad h<r<1. \tag{3.21}$$

For the pressure field:

$$p(r,z) = \frac{\omega^2}{2\pi}\int_\Gamma \frac{(1-uM_0)^2F_+(u)}{\lambda_0} T_0(r,u)\exp(\mathrm{i}\omega u z)\,\mathrm{d}u, \quad r>1, \tag{3.22}$$

$$p(r,z) = \frac{\omega^2 D_1}{2\pi}\int_\Gamma \frac{(1-uM_1)^2F_+(u)}{\lambda_1} T_1(r,u)\exp(\mathrm{i}\omega u z)\,\mathrm{d}u, \quad h<r<1, \tag{3.23}$$

where we have used

$$T_0(r,u) = \frac{\mathrm{H}_m^{(1)}(\lambda_0\omega r)}{\mathrm{H}_m^{(1)\prime}(\lambda_0\omega)}, \quad T_1(r,u) = \frac{\mathrm{Y}_m'(\lambda_1\omega h)\mathrm{J}_m(\lambda_1\omega r) - \mathrm{J}_m'(\lambda_1\omega h)\mathrm{Y}_m(\lambda_1\omega r)}{\mathrm{Y}_m'(\lambda_1\omega h)\mathrm{J}_m'(\lambda_1\omega) - \mathrm{J}_m'(\lambda_1\omega h)\mathrm{Y}_m'(\lambda_1\omega)}.$$

For non-uniform flows, the instability wave is described by the simple pole u_0 of F_+. The following expression of the instability wave is obtained by taking the residue of this pole:

$$\psi(r,z) = \omega\exp(\mathrm{i}\omega u_0 z)\operatorname*{Res}_{u\to u_0}[F_+(u)]\mathrm{H}(z)\begin{cases}(1-uM_0)T_0(r,u_0)/\lambda_0,\\ (1-uM_1)T_1(r,u_0)/\lambda_1,\end{cases} \tag{3.24}$$

$$p(r,z) = \mathrm{i}\omega^2\exp(\mathrm{i}\omega u_0 z)\operatorname*{Res}_{u\to u_0}[F_+(u)]\mathrm{H}(z)\begin{cases}(1-uM_0)^2T_0(r,u_0)/\lambda_0,\\ D_1(1-uM_1)^2T_1(r,u_0)/\lambda_1,\end{cases} \tag{3.25}$$

where H is the Heaviside function. The residue of F_+ at u_0 is

$$\operatorname*{Res}_{u\to u_0}[F_+(u)] = -\gamma\Psi_{mn}(1)D_1(1-\mu_{mn}^+M_1)\frac{\lambda_0^-(\mu_{mn}^+)\lambda_1^-(\mu_{mn}^+)\tilde{K}_-(\mu_{mn}^+)\lambda_0^+(u_0)\lambda_1^+(u_0)}{\omega(\mu_{mn}^+-u_0)\tilde{K}_+(u_0)}.$$

This shows how the parameter γ controls the amplitude of the vorticity shedding.

The numerical evaluation of the solution presented in this section is not straightforward, the critical issues being the evaluation of the split functions $\tilde{K}_\pm$ and the inverse Fourier transforms (3.20)–(3.23). A detailed description of the numerical implementation of the model is given in Appendix A.

3.4. *Far-field approximation*

The directivity pattern far away from the duct termination is a convenient way to describe the sound radiated out of the duct. This approximation also reduces significantly the cost of numerical evaluation compared to the general solutions

(3.20)–(3.23) involving inverse Fourier transforms. The solution in the far field is obtained by taking the limit $\omega R \to +\infty$ and by making use of the stationary phase approximation, details can be found in Rienstra (1984). Both solutions (3.20) and (3.22) are of the form

$$q(r,z) = \frac{\omega}{2\pi}\int_{\Gamma} Q(u)\mathrm{H}_m^{(1)}(\lambda_0\omega r)\exp(\mathrm{i}\omega u z)\,\mathrm{d}u, \tag{3.26}$$

where q is either the pressure or the velocity potential and Q is easily identified in (3.20) or (3.22). The solution in the far field is found to be

$$q(R,\Theta) = \frac{Q(u_s)}{\pi R\left(1-M_0^2\sin^2\Theta\right)^{1/2}}\exp\left[\mathrm{i}\omega R S(\Theta) - \mathrm{i}(m+1)\frac{\pi}{2}\right], \tag{3.27}$$

where we have introduced the spherical coordinates R, Θ defined by $z = R\cos\Theta$ and $r = R\sin\Theta$. The function S accounts for the wavefront stretching produced by the ambient flow: $S(\Theta) = [(1-M_0^2\sin^2\Theta)^{1/2} - M_0\cos\Theta]/(1-M_0^2)$. The stationary point u_s of the integral (3.26) is given by $u_s = (\cos\hat{\Theta} - M_0)/(1-M_0^2)$ with $\hat{\Theta} = \tan^{-1}[(1-M_0^2)^{1/2}\tan\Theta]$. The directivity functions D_p and D_ψ for the pressure and velocity potential are defined as $D_p(\Theta) = |p|R$ and $D_\psi(\Theta) = |\psi|R$, respectively.

3.5. *Reflection coefficients*

The derivation of the reflection coefficients used in the present work follows that of Rienstra (1984) and only the main results are given here. The modal decomposition of the pressure field inside the duct can be written as follows:

$$p(r,z,\theta,t) = \sum_{m=-\infty}^{+\infty}\sum_{n=0}^{+\infty}[A_{mn}^- \exp(\mathrm{i}\omega\mu_{mn}^- z) + A_{mn}^+\exp(\mathrm{i}\omega\mu_{mn}^+ z)]\Psi_{mn}(r)\exp(\mathrm{i}m\theta - \mathrm{i}\omega t), \tag{3.28}$$

where $A_{mn}^{\pm}$ are the amplitudes of the pressure modes. The reflection coefficients are then defined as $R_{mnl} = A_{ml}^-/A_{mn}^+$. The incident wave was defined as one single mode (m,n) with the corresponding velocity potential given by (2.11). Upon using (2.4), we find $A_{mn}^+ = \mathrm{i}\omega D_1(1-\mu_{mn}^+ M_1)$.

The pressure inside the duct is given by (3.23) with $z<0$. Evaluating the residues of the poles of the integrand lying below the integration path Γ yields an expression similar to the modal decomposition (3.28) and we can identify the pressure mode amplitudes:

$$A_{00}^- = \frac{\mathrm{i}\omega D_1(1-\mu_{00}^- M_1)^2 F_+(\mu_{00}^-)}{C_1(1-h^2)}, \quad A_{ml}^- = \frac{\mathrm{i}\omega D_1(1-\mu_{ml}^- M_1)^2 F_+(\mu_{ml}^-)}{\Lambda'(\alpha_{ml})\left[M_1 C_1^2 + \mu_{ml}^-\left(1-M_1^2C_1^2\right)\right]}. \tag{3.29}$$

3.6. *Expressions for a hollow duct*

The expressions for a duct with circular cross-section, i.e. without centre body, are obtained by taking the limit $h \to 0$. The mode shapes of the incident wave (2.11) and the modal decomposition (2.9) are now written $\Psi_{mn}(r) = \mathrm{J}_m(\alpha_{mn}r)$ where α_{mn} is a solution of the characteristic equation $\Lambda(z) = \mathrm{J}_m'(z) = 0$. The solution (3.4) for β is $\beta(r,u) = B(u)\mathrm{J}_m(\lambda_1\omega r)$ for $r<1$, therefore equations (3.8) and (3.9) become, respectively:

$$-\mathrm{i}(1-uM_1)F_+(u) = B(u)\lambda_1\mathrm{J}_m'(\lambda_1\omega),$$

$$G(u) = -\mathrm{i}\omega[(1-uM_0)A(u)\mathrm{H}_m^{(1)}(\lambda_0\omega) - D_1(1-uM_1)B(u)\mathrm{J}_m(\lambda_1\omega)].$$

The definition (3.12) of the Wiener–Hopf kernel is now:

$$K(u) = D_1(1-uM_1)^2\lambda_0\frac{\mathrm{J}_m(\lambda_1\omega)}{\mathrm{J}'_m(\lambda_1\omega)} - (1-uM_0)^2\lambda_1\frac{\mathrm{H}^{(1)}_m(\lambda_0\omega)}{\mathrm{H}^{(1)\prime}_m(\lambda_0\omega)}. \tag{3.30}$$

The general solutions (3.20)–(3.25) remain unchanged, but with $T_1(r,u) = \mathrm{J}_m(\lambda_1\omega r)/\mathrm{J}'_m(\lambda_1\omega)$. For the reflected pressure mode amplitudes (3.29), we now have $\Lambda'(\alpha_{ml}) = \mathrm{J}''_m(\alpha_{ml})$ and $h = 0$.

4. Results

Much of the usefulness of the current model rests upon whether it can be applied to turbofan exhausts at realistic frequencies and flow conditions. With this in mind, results are presented for a base set of non-dimensional parameters typical of a modern turbofan engine at blade passing frequency while operating in the 'cut-back' condition. The hub–tip ratio, jet Mach number and free-stream Mach number are defined as $h = R_1/R_0 = 0.75$, $M_1 = v_j/c_0 = 0.45$ and $M_0 = v_0/c_0 = 0.25$, respectively. The density and speed of sound are uniform, $C_1 = D_1 = 1$. The non-dimensional frequency is taken to be $\omega = 30$. In dimensional terms, this corresponds to '$ka = 30$' where k is the free-field wavenumber (= radian frequency/sound speed) and a is the outer radius of the duct. Initially, the full Kutta condition ($\gamma = 1$) is used to describe the vortex shedding at the trailing edge, i.e. all the available vorticity is shed from the trailing edge.

4.1. *Validation*

Several checks can be performed to validate the present model.

In the absence of a centre body ($h = 0$), Munt (1977) has calculated far-field directivity patterns, mainly for the plane wave mode (0,0) at frequencies up to $\omega = 11.7$. These published data have been compared to results obtained by the current procedure and found to be in agreement.

Energy conservation provides another check on the validity of the model; specifically whether the acoustic power inside the duct is equal to the radiated acoustic power in the far field. Some care must be taken in making this comparison however. It is not valid when vortex shedding occurs ($\gamma \neq 0$) since the vortex sheet then generates hydrodynamic waves which can either add energy to, or subtract it from the acoustic field – this issue has been discussed by Rienstra (1981, 1984). The acoustic power associated with the modal decomposition (2.9) inside the duct can be written (Goldstein 1976):

$$P = \pi\omega^2 D_1 \sum_m \sum_n C_{mn}\sqrt{C_1^2 - \left(1 - M_1^2 C_1^2\right)\alpha_{mn}^2/\omega^2}\int_h^1 |\Psi_{mn}(r)|^2 r\,\mathrm{d}r,$$

where $C_{mn} = |B^+_{mn}|^2 - |B^-_{mn}|^2$ for cut-on modes and $C_{mn} = B^+_{mn}\overline{B^-_{mn}} - B^-_{mn}\overline{B^+_{mn}}$ for cut-off modes. Furthermore, the acoustic radial intensity I_R in the far field can be obtained from the directivity of the velocity potential:

$$I_R(R,\Theta) = \frac{\omega^2|D_\psi(\Theta)|^2}{2R^2\sqrt{1 - M_0^2\sin^2(\Theta)}}.$$

The above expressions have been evaluated for the base set of non-dimensional parameters noted at the beginning of this section, and the radiated acoustic power and the in-duct power have been found to be the same for cut-on modes when vortex shedding is absent ($\gamma = 0$).

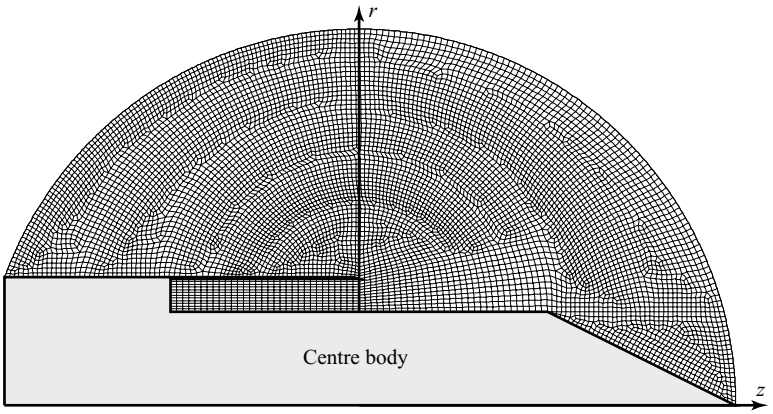

FIGURE 3. Finite-element mesh used for the comparison with a finite-length after-body.

The ability of the current solution to model scattering by the centre body cannot be validated by comparison to Munt's results. This aspect of the solution can, however, be checked in the absence of flow by comparing the analytic solution to results obtained from a high-resolution numerical model. A solution of this type has been computed by using the commercial finite/infinite element code Actran (Free Field Technologies 2004). The finite element (FE) mesh which was used is shown in figure 3. Note that the after body is truncated to fit within the FE domain, being terminated by a conical end cap. Quadratic isoparametric finite elements were used together with high-order infinite elements to model radiation to the far field. Once again the comparison is made for the base set of non-dimensional parameters noted at the start of this section, but with the Mach number set to zero.

Far-field pressure directivity patterns given by the analytical and the numerical models are compared in figure 4. Results are presented for the (4,0), (17,0) and (24,0) modes. These are representative of a well cut-on mode, an intermediate mode and an almost cut-off mode, respectively (recall the mode orders m and n start at 0). The two predictions are generally in excellent agreement although in the case of the well cut-on (4,0) mode the directivity pattern exhibits oscillations associated with diffraction of wave field by the conical end-cap. This effect is not significant for the other modes since the acoustic energy is scattered away from the axis close to the duct exit. This leads to an observation that, at this frequency, the infinite centre body of the analytic solution appears to be a reasonable model for a finite after-body of the type that might be encountered in real turbofan applications.

4.2. *Parametric study*

Taking the parameters noted at the start of this section as a 'baseline' configuration, a parametric study is presented to investigate the extent to which the far-field directivity is sensitive to variations of the external flow velocity, the hub–tip ratio and the degree of vortex shedding at the duct exit.

4.2.1. *The noise source in the duct*

Noise propagating in the bypass duct of a turbofan engine contains both tone and broadband components. The tone component is dominated at higher tip speeds by rotor-locked harmonics of the blade passage frequency and at lower speeds by a less well defined sequence of rotor–stator interference tones. The effect of parametric

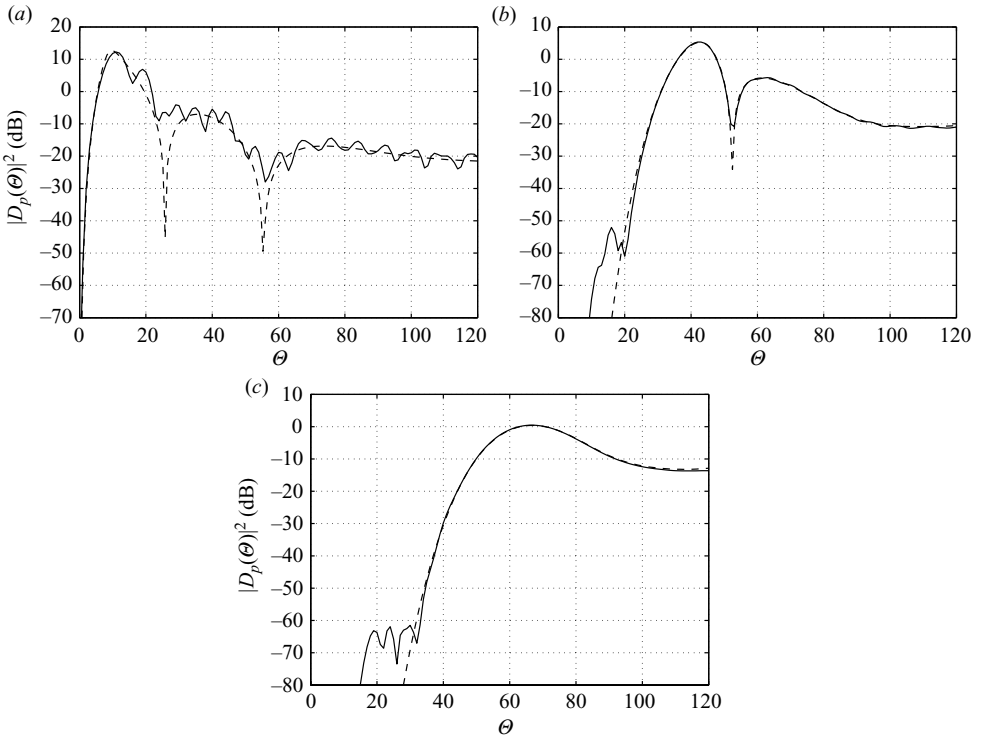

FIGURE 4. Comparison of the pressure directivity patterns in the far field $|D_p(\Theta)|^2$ in dB: Finite-element solutions (solid line); analytical solutions (dashed line). Parameters are $h = 0.75$, $M_0 = M_1 = 0$, $C_1 = D_1 = 1$, $\gamma = 0$, $\omega = 30$. (*a*) Mode (4,0); (*b*) mode (17,0); (*c*) mode (24,0).

changes on the radiation of tone noise to the far field will be characterized here by an analysis of far-field directivity patterns for specific incident modes (m,n) in the duct. In all instances, the far-field directivity is normalized for unit incident modal power.

The broadband component of the noise in the duct is generated by turbulence which forms in the boundary layer of each blade and interacts with the trailing edge and with the stators. This will be represented in the current study by a multi-mode field in which all cut-on modes are present with equal modal power and the total incident power is set equal to unity. The pressure directivity pattern in the far field is obtained by assuming that the modes are uncorrelated and by summing the corresponding pressure directivity patterns. These must be calculated independently. For the baseline configuration, there are 149 cut-on modes. By using the symmetry of positive and negative circumferential mode orders, this reduces to 76 independent directivity patterns for each set of parameters.

4.2.2. *The effect of ambient Mach number*

First, consider the effect of varying the external flow velocity. This is done by setting $M_0 = 0.0$, 0.15, 0.25, 0.35 and 0.45 while holding other baseline parameters constant. The extreme cases $M_0 = 0$ and $M_0 = 0.45$ then correspond to a static engine test in which the ambient fluid is at rest, and to a flight condition in which there is no flow discontinuity at the edge of the jet. Figure 5 shows the directivity patterns of the pressure for three single tones and for the 'broadband' sum of all uncorrelated cut-on modes. The modes (4,0), (17,1) and (24,1) are chosen to characterize tone sources.

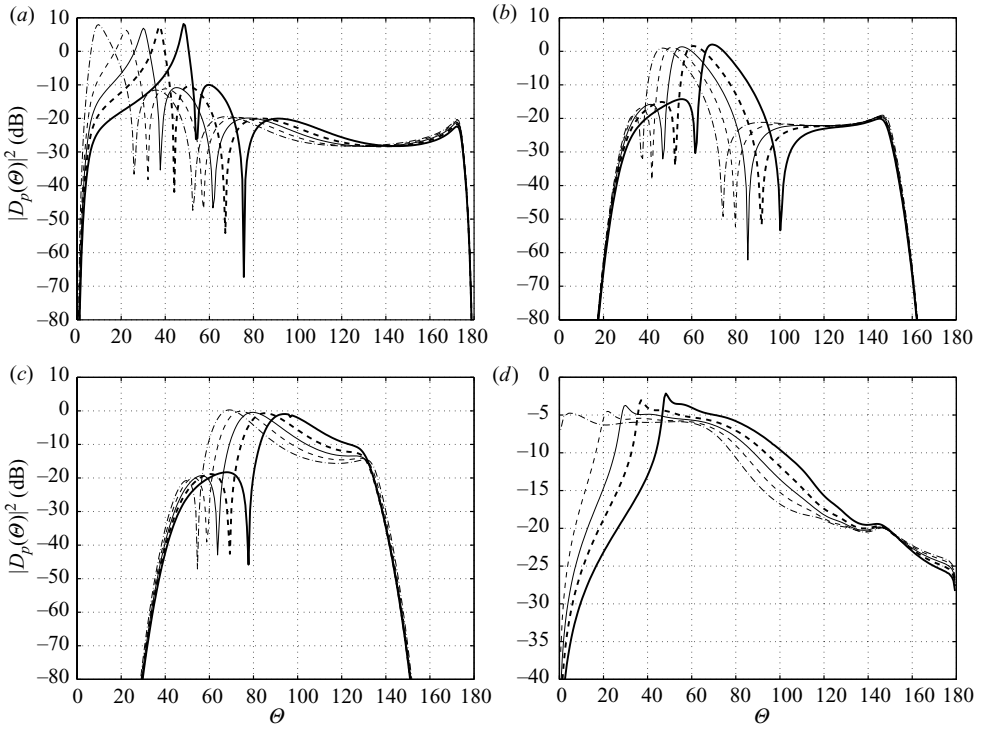

FIGURE 5. Pressure directivity patterns in the far field $|D_p(\Theta)|^2$ in dB with $M_0 = 0$ (thick solid line), 0.15 (thick dashed line), 0.25 (thin solid line), 0.35 (thin dashed line) and 0.45 (thin dot-dashed line). (*a*) (4,0) mode. (*b*) (17,1) mode. (*c*) (24,1) mode. (*d*) Broadband multi-mode source. Other parameters are $h = 0.75$, $M_1 = 0.45$, $C_1 = D_1 = 1$, $\gamma = 1$, $\omega = 30$.

As the Mach number of the ambient stream decreases from $M_0 = 0.45$ to $M_0 = 0$, the refraction of acoustic waves produced by the velocity mismatch at the vortex sheet increases and shifts the lobe of the directivity patterns away from the jet axis. A cone of silence appears between the first lobe and the jet axis where the pressure level decreases sharply. For the static test case ($M_0 = 0$) this extends for approximately 50° from the jet axis.

The directivity patterns for the multi-mode broadband source do not exhibit lobes since the summation over all the cut-on modes tends to smooth out the minimums and maximums observed with the directivity patterns of single modes. However, three different regions can be considered. The aft direction corresponds to the cone of silence where the pressure level decreases rapidly as the external Mach number M_0 is reduced. The peak of acoustic radiation is found at the limit between the cone of silence and an intermediate region where the pressure increases with decreasing M_0, a refractive effect which deviates more energy towards the intermediate region. Finally, in the forward arc (from 150° to 180°), a third region exists where the pressure level decreases with M_0, of little practical significance given these levels are 20–30 dB down on the peak values.

When comparing flight test ($M_0 = 0.25$) and static test ($M_0 = 0$) data, we observe that the peak of acoustic radiation is increased by approximately 2 dB and moves forward by approximately 20°.

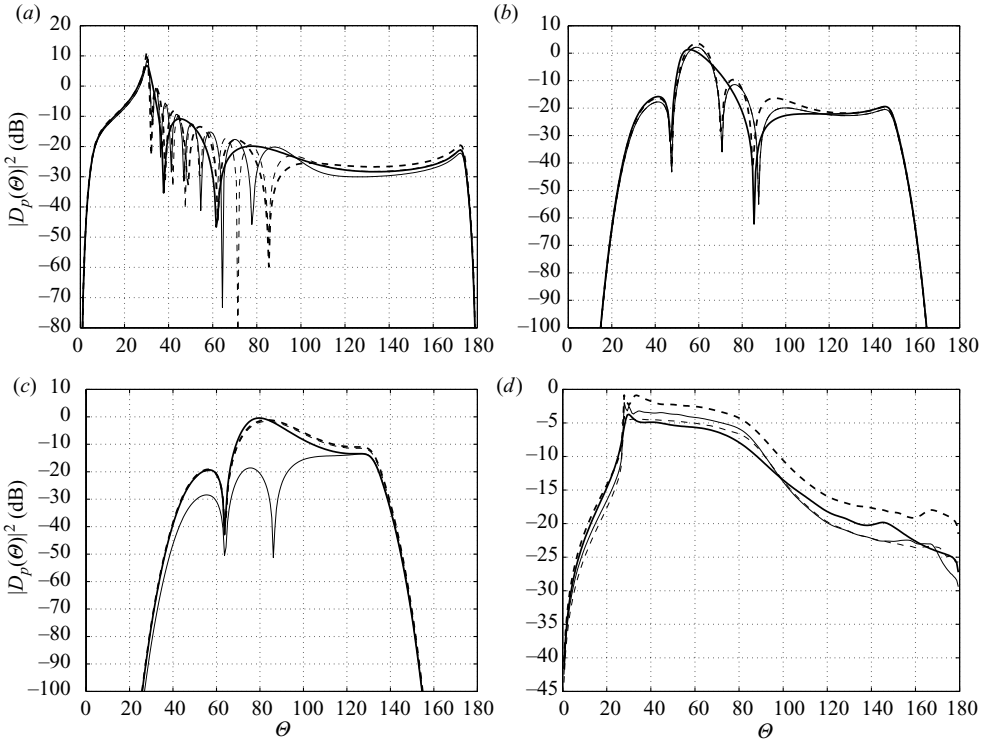

FIGURE 6. Pressure directivity patterns in the far field $|D_p(\Theta)|^2$ in dB with $h = 0$ (thick solid line), 0.25 (thick dashed line), 0.5 (thin solid line) and 0.75 (thin dashed line). (*a*) (4,0) mode. (*b*) (17,1) mode. (*c*) (24,1) mode. (*d*) Broadband multi-mode source. Other parameters are $M_0 = 0.25$, $M_1 = 0.45$, $C_1 = D_1 = 1$, $\gamma = 1$, $\omega = 30$.

4.2.3. *The effect of the centre body*

We now consider the effect of the centre body by varying the hub–tip ratio from $h = 0.75$ to $h = 0$ in steps of 0.25 (figure 6). The upper value corresponds to the base configuration while the lower value $h = 0$ corresponds to a hollow circular duct with no centre body at all. Note that the modes are normalized so that the same amount of acoustic energy propagates inside the duct irrespective of the size of the centre body. For low-order modes such as (4,0), reduction of the hub–tip ratio simply causes more radial modes to propagate and results in a directivity pattern with more lobes. For higher-order modes, (17.1) and (24,1), this effect is still present, but less pronounced. In the case of the (24,1) mode, the large reduction in radiated sound and dramatic change in directivity for $h = 0.25$ arises because the third radial mode is about to cut-on and significant reflections occur at the duct exit.

In the case of the equal power broadband source, it is not possible to find a general trend as the hub–tip ratio varies. For instance, the overall pressure level increases by 3 dB as h changes from 0.75 to 0.5, but then decreases for $h = 0.25$. Once again this reflects the fact that, as h varies, the number of cut-on modes as well as their cut-off ratio changes and the proportion of energy reflected back into the duct is dependent on the proximity of any modes to their cut-on frequency. The larger pressure levels observed for the case $h = 0.5$, for example, can be explained by the fact that, in that case, fewer modes are close to their cut-off frequencies and so more energy is radiated in the far field.

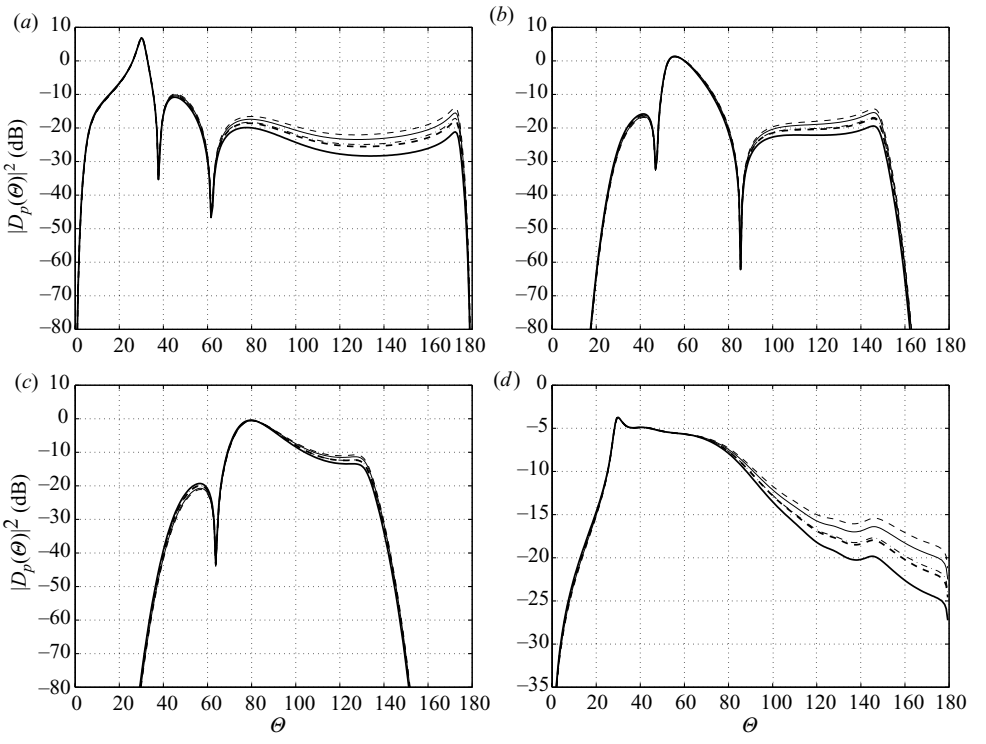

FIGURE 7. Pressure directivity patterns in the far field $|D_p(\Theta)|^2$ in dB with $\gamma = 1$ (thick solid line), 0.5 (thick dashed line), 0 (thin solid line), i (thin dashed line) and $e^{i\pi/4}$ (thin dot-dashed line). (*a*) (4,0) mode. (*b*) (17,1) mode. (*c*) (24,1) mode. (*d*) Broadband multi-mode source. Other parameters are $h = 0.75$, $M_0 = 0.25$, $M_1 = 0.45$, $C_1 = D_1 = 1$, $\omega = 30$.

4.2.4. *The effect of shed vorticity – the Kutta condition*

Finally, we consider the effect on the radiated sound field of vorticity shed from the lip of the duct. The amount of shed vorticity is defined by the complex parameter γ. Results are presented for $\gamma = 1$, 0.5 and 0 and for $\gamma = \mathrm{i}$ and $\mathrm{e}^{\mathrm{i}\pi/4}$. Other parameters are again held constant. The resulting far-field directivities for tone and broadband incident fields are shown in figure 7. The extent of vortex shedding is found to have virtually no effect on the main lobe of the directivity patterns, but is noticeable in the rear arc where the sound pressure level increases as the amplitude of γ decreases and as its phase increases. In the case of a broadband multi-mode source, the effect of varying γ is minimal, less than 1 dB over the whole forward arc. In terms of predicting the direction and magnitude of the principal radiation lobe, these results suggest that the effect on the acoustic field of vorticity shed from the lip of the duct is largely negligible. This is not necessarily true at lower frequencies and indeed Rienstra (1983) has indicated that at small Strouhal numbers, vortex shedding has a more significant impact on acoustic radiation.

4.3. *Comparisons with experimental data*

It is also important to check how the predictions of the analytical model compare with experimental measurements for a similar configuration. However, in the literature, the problem of aft fan noise radiation in the presence of a jet and an after-body has rarely been studied experimentally. A notable exception is the active noise control

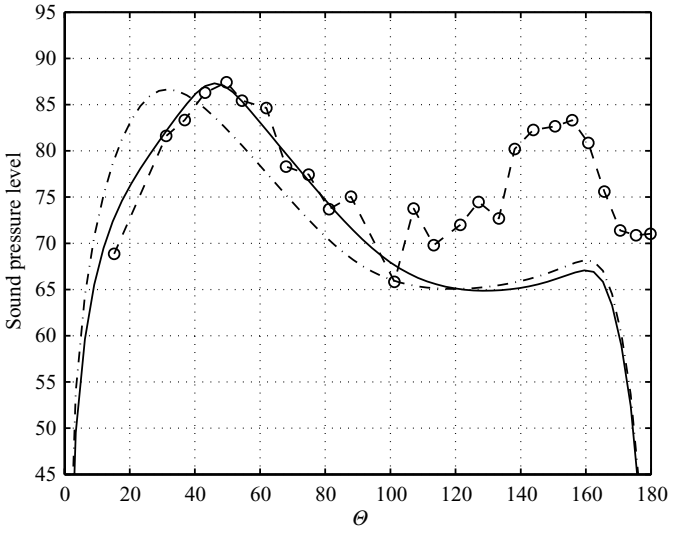

FIGURE 8. Sound pressure level at 40 ft from the exhaust. Solid line: analytical solution; Dashed line: experimental data from the ANCF test rig; Dot-dashed line: analytical solution with a uniform flow.

fan rig (ANCF) developed at NASA Glenn Research Center. The ANCF is a 48 in diameter straight duct with a 16 blade rotor operating in the range of 1500 to 2000 r.p.m. As the diameter of the centre body varies along the duct the hub–tip ratio varies from 0.3 at the stator plane to 0.5 at the exhaust plane. The ambient air is at rest and the Mach number inside the duct varies from 0.13 at the inlet to 0.175 at the exhaust. The spinner extends far beyond the duct exit plane and can be modelled as an infinite centre body. In-duct measurements were made using a rotating rake system to determine the mode amplitudes at the inlet and exhaust sections. This set-up is located in an anechoic chamber where the far-field directivity is measured. Detailed descriptions of the ANCF test rig can be found in Sutliff *et al.* (1996*a*,*b*).

Comparisons are made at 2000 r.p.m. with 14 blade vanes. For this configuration, the interference tone (2,0) is dominant both at the inlet and exhaust planes so only this mode is included in the analytical solution. Figure 8 compares the experimental and theoretical sound pressure levels in the far field at 40 ft from the duct exit plane. Good agreement is observed between predicted and measured solutions in the 'rear' arc of the rig (i.e. $\theta \leqslant \pi/2$, where θ is measured from the exhaust axis) where radiation from the bypass duct is the dominant contributor. This holds both for the directivity and the absolute level. In the 'forward' arc ($\theta > \pi/2$), noise radiated from the rig intake dominates the overall sound field, and the comparison with predicted aft radiated noise is no longer appropriate. The correspondence in the rear arc indicates, however, that the analytical model captures well the physics of the sound radiation through the exhaust stream.

Also given in figure 8 is the sound pressure level computed in the far field with a uniform mean flow (the ambient flow is the same as the jet). The low Mach number jet is found to have a significant effect on the directivity since the change in the mean flow shifts the directivity peak by approximately 15°. This illustrates how crucial it is to account for the refraction effect of the shear layer in order to obtain accurate predictions.

4.4. *Near-field solutions*

The numerical procedures for evaluating the solution which are detailed in Appendix A are sufficiently efficient to be used to determine field values at an adequate number of near-field points to permit the construction of near-field contour maps of the acoustic pressure. By using the techniques described in Appendix A, this can be done at modest computational cost, that is to say, minutes rather than hours of process time on a single 32 bit PC processor. The results of such a computation are shown in figures 9 and 10. In figure 9, the real part of the near field pressure is shown for the acoustic portion of the solution calculated for the three representative tones which have been used in the parametric study, i.e. modes (4,0), (17,1) and (24,1). The pressure fields corresponding to the instability solution for the same incident modes are shown in figure 10. The full solution (not shown) is obtained by superimposing the two contributions. Note that the dynamic continuity condition – equation (2.8) – holds at the vortex sheet, and the pressure fields are therefore continuous even when vorticity is shed from the trailing edge. The velocity potential, which has not been plotted here, is, however, discontinuous across the vortex sheet when $\gamma \neq 0$.

Turning to the acoustic fields themselves, it can be seen that the near-field solutions strongly differ from the far-field directivity patterns given in figure 5, the diffraction effect being less significant in the near field. Also, the reflection of waves inside the duct from its open end is clearly visible, particularly for modes (17,1) and (24,1) which are less well cut-on.

The instability waves given in figure 10 emanate from the trailing edge and grow exponentially in the streamwise direction. However, their amplitude decreases exponentially as we move away from the vortex sheet. The combination of these two effects means that the instability solution is confined in a type of double conical zone around the cylindrical vortex sheet. Beyond this region, the amplitude of the instability solution is negligible. The angular span of this zone in a generating plane through the axis of the jet, is defined by an angle $\Theta^\star$, where $\Theta^\star$ is given by $\tan\Theta^\star = -\mathrm{Im}(u_0)/\mathrm{Im}(\lambda_0)$. This result is obtained by using the asymptotic form of the Hankel function in the expression (3.25) for the instability wave. This yields a factor $\exp[\mathrm{i}\omega(u_0 z + \lambda_0 r)]$ in (3.25) and the angle $\Theta^\star$ represents the direction where $u_0 z + \lambda_0 r$ is real.

However, it should be emphasized that the exponential growth of the instability wave far away from the trailing edge is not realistic, being an artefact of the linear theory used in the model. In practice, the growth of instability waves in the vortex sheet is rapidly saturated by nonlinear effects which subsequently produce vortices. This results in the growth of the mixing layer downstream of the trailing edge which is not described in the present model.

5. Conclusion

The model presented in this paper is capable of providing far-field directivity patterns, reflection coefficients and near-field solutions for the radiation of acoustic waves from an annular jet pipe. The model incorporates the interactions of the acoustic field with the vortex sheet as well as the presence of an infinite centre body. It is exact within the limits of linear theory. It serves as an idealized model for the sound radiated from the bypass duct of a turbofan engine and has been used in this mode to predict the far-field directivity patterns for single tones and multi-mode sources for frequency, geometry and flow parameters characteristic of a modern HBR engine at maximum power. These results demonstrate the effect of the external flow, hub–tip ratio and vortex shedding on sound radiation. The latter effect, in particular,

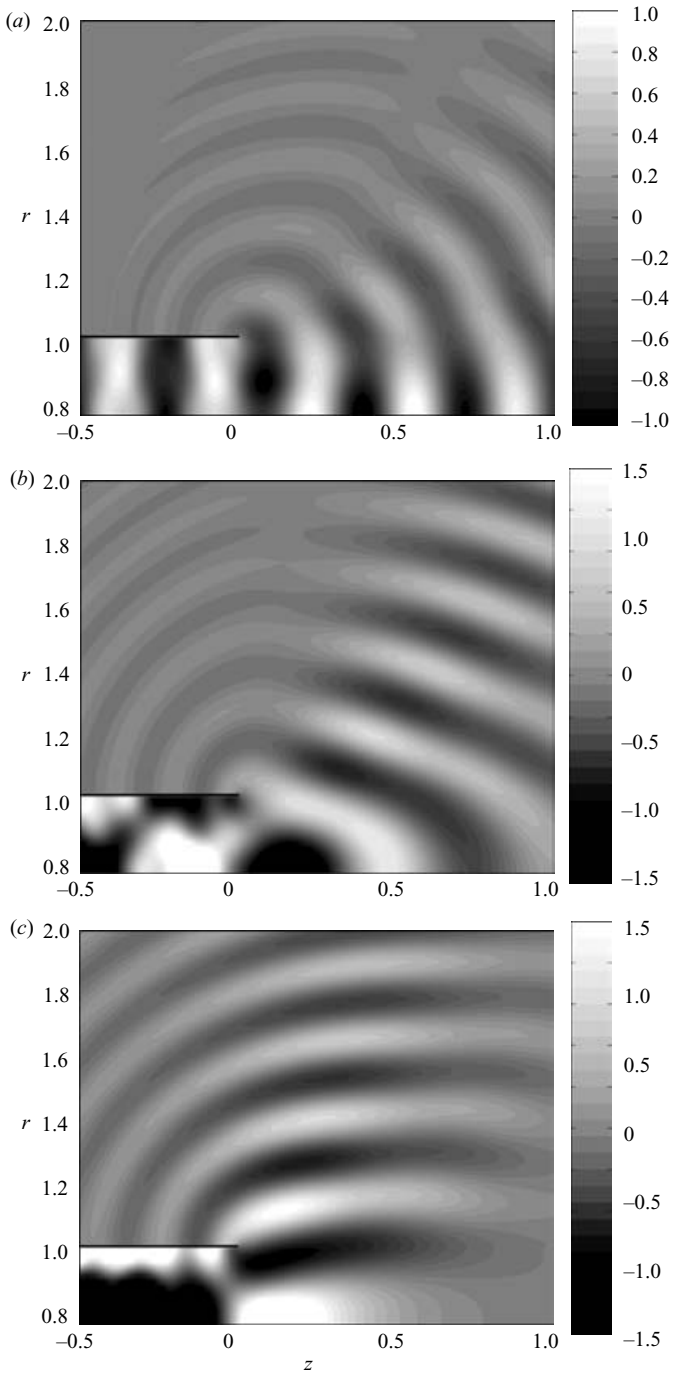

FIGURE 9. Real part of the acoustic pressure field in the near field. (*a*) Mode (4,0); (*b*) mode (17,1); (*c*) mode (24,1). Parameters are $h = 0.75$, $M_0 = 0.25$, $M_1 = 0.45$, $C_1 = D_1 = 1$, $\gamma = 1$, $\omega = 30$.

is found to have little impact on the peak of acoustic radiation, suggesting that vorticity shedding may be ignored if we are only concerned with the direction and magnitude of the maximum radiation lobe.

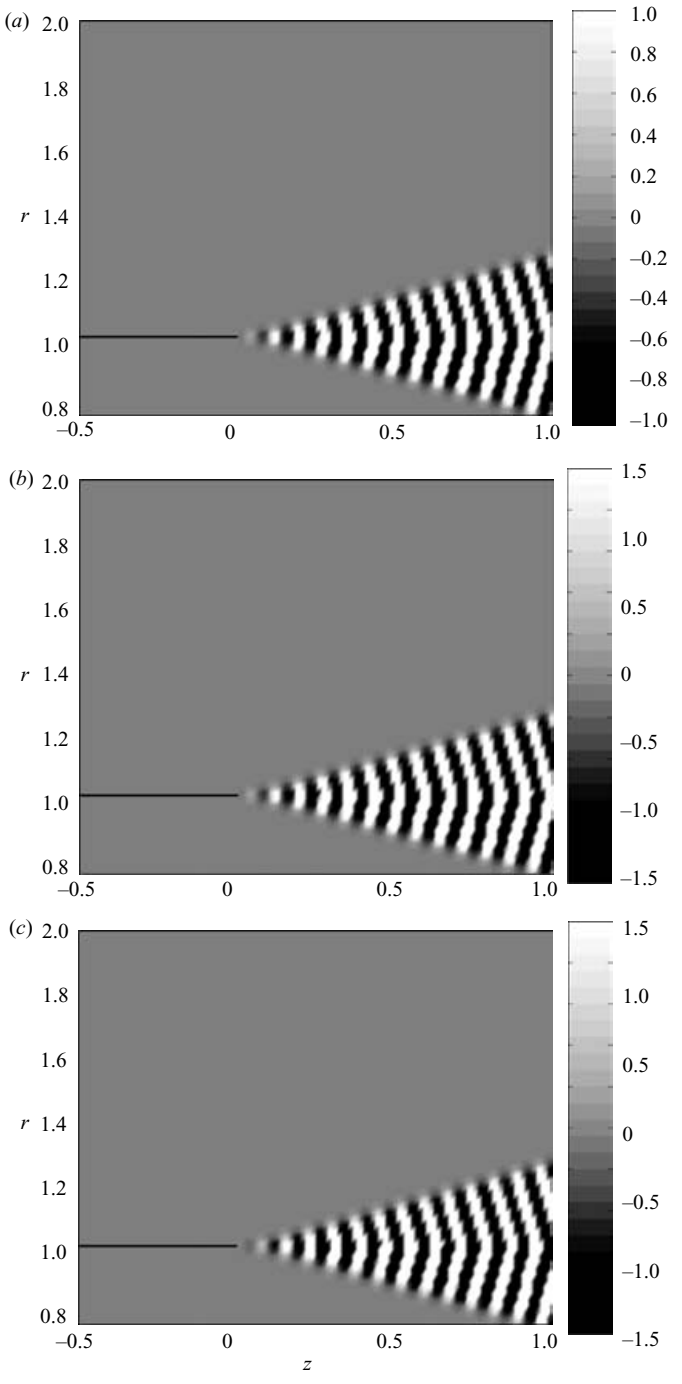

FIGURE 10. Real part of the pressure field for the instability wave in the near field. (*a*) Mode (4,0); (*b*) mode (17,1); (*c*) mode (24,1). Parameters are $h = 0.75$, $M_0 = 0.25$, $M_1 = 0.45$, $C_1 = D_1 = 1$, $\gamma = 1$, $\omega = 30$.

An original feature of the present model is that it is able to evaluate the exact solutions in the near field. Therefore, it is well suited as a general benchmark problem for computational aero-acoustics (CAA). This aspect of the solution has not been

emphasized in this paper. It is worth noting, however, that it embodies many of the challenging features that must be faced by CAA codes, and deals with them without approximation. These include scattering by rigid surfaces, radiation to the far field, refraction through a mixing layer and the presence of instability waves (Gabard, Astley & Tahar 2005).

An obvious extension to the current model which has not been considered at this stage, but which could be investigated in the future, is its reformulation to include inner and outer jets with a view to modelling the acoustic radiation through co-axial jets. However, according to the work by Taylor *et al.* (1993) on buried nozzles, deriving a solution for coaxial jets is difficult since it involves the factorization of matrix Wiener–Hopf kernels.

The present work was conducted at the Institute of Sound and Vibration Research (Southampton, UK) in the framework of the European Doctorate in Sound and Vibration Studies under the Marie Curie Fellowship Scheme. The authors acknowledge E. Envia of NASA Glenn Research Center for providing experimental data from the ANCF test rig. The authors have also benefited from useful discussions with S. W. Rienstra, P. Joseph and B. J. Tester. The ACTRAN simulations presented in this paper were carried out by L. de Mercato.

Appendix A. Numerical methods

A.1. *Evaluation of the split functions*

The major difficulty in solving the Wiener–Hopf equation (3.11) is to find split functions $\tilde{K}_\pm$ such that $\tilde{K}_+(u)/\tilde{K}_-(u) = K(u)/(u-u_0)^b$ and with $\tilde{K}_\pm$ regular and non-zero in $R_\pm$. We only need to consider the evaluation of $\tilde{K}_+(u)$, since we have $\tilde{K}_-(u) = \tilde{K}_+(u)(u-u_0)^b/K(u)$.

For simple problems, it is possible to find analytical expressions for $\tilde{K}_\pm$ and Noble (1958) contains many examples of problems where an explicit factorization of the kernel is amenable. This is not the case for the problem at hand, and the split function is evaluated using the following general factorization formula:

$$\log \tilde{K}_+(u) = \frac{-1}{2\mathrm{i}\pi}\int_C \frac{\log[K(\zeta)/(\zeta-u_0)^b]}{\zeta-u}\,\mathrm{d}\zeta, \tag{A 1}$$

where the path of integration C goes from $-\infty \mathrm{e}^{-\mathrm{i}\epsilon}$ to $+\infty \mathrm{e}^{-\mathrm{i}\epsilon}$ in the strip S, crosses the real axis at u_c and lies above u. As $\epsilon \to 0$, the width of the strip S is going to zero and S is located above the negative real axis and below the positive real axis. Unlike the path of integration Γ for the inverse Fourier transform (3.19), the path C does not need to be indented around the zero u_0 of K since $\tilde{K}_\pm$ are split functions of $K(u)/(u-u_0)^b$ which does not have a zero at u_0.

First, we should note that it is not clear whether the integral in (A 1) should converge. To obtain convergence, the boundary of the integral should be sent to infinity simultaneously and, for numerical purposes, it is convenient to fold the integration on a semi-infinite contour going from u_c to $+\infty - 0\mathrm{i}$. By using $\zeta = u_c - v$ for $\mathrm{Re}(\zeta) < u_c$ and $\zeta = u_c + v$ for $\mathrm{Re}(\zeta) > u_c$, we can write

$$\log \tilde{K}_+(u) = \frac{-1}{2\mathrm{i}\pi}\int_0^{+\infty-0\mathrm{i}} \left\{ \frac{\log[K(u_c-v)/(u_c-v-u_0)^b]}{u_c-v-u} + \frac{\log[K(u_c+v)/(u_c+v-u_0)^b]}{u_c+v-u} \right\} \mathrm{d}v. \tag{A 2}$$

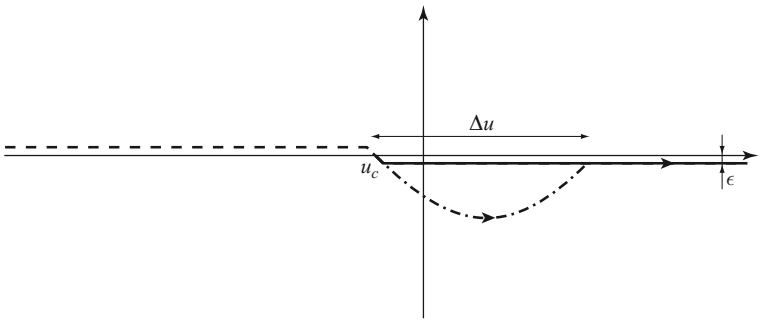

FIGURE 11. Contours of integration for the numerical evaluation of the split function K_+: the original path C_+ from $u = -\infty + 0\mathrm{i}$ to $+\infty - 0\mathrm{i}$ (dashed line), the folded path from $u = u_c$ to $+\infty - 0\mathrm{i}$ (solid line) and the deformed path from $u = u_c$ to $+\infty - 0\mathrm{i}$ (dot-dashed line).

Furthermore, several zeros and poles of the kernel lie on the real axis between the branch cuts. So, when the contour of integration is in this region of the complex plane, the integrand exhibits steep variations which make the numerical evaluation of the integral expensive. To avoid this problem and accelerate the numerical integrations, Rienstra (1984) proposed to deform the contour so that it lies as far as possible from these poles and zeros on the real axis. The deformed contour is shown in figure 11 and is made of a parabola from $v = 0$ to $\Delta u - \mathrm{i}\varepsilon$ and then a straight line from $v = \Delta u - \mathrm{i}\varepsilon$ to $+\infty - \mathrm{i}\varepsilon$. The parabola is chosen to be

$$v(\kappa) = \kappa + \mathrm{i}\left(\frac{\Delta u - \varepsilon}{\Delta u^2}\kappa^2 - \kappa\right).$$

The use of the deformed contour leads to a significant reduction of the time for the numerical evaluation (a factor of 3–4 has been observed). For the numerical evaluation, the upper boundary of the integral is taken to be a large value, A say, so that the remaining part of the integral (from A to $+\infty$) is negligible. Finally, for $\tilde{K}_+$, we have to check that u is below the contour of integration. If this is not the case, we have to add the contribution of the pole corresponding to $\zeta = u$ in (A 1).

Also, the location of the zero u_0 is required to evaluate equation (A 1). It is obtained with standard algorithms for solving nonlinear equations with an initial guess given by the high-frequency approximation (3.13).

A.2. *Evaluation of the kernel*

As explained in the previous section, we must evaluate the kernel (3.12) or (3.30) for a large range of parameter u in the complex plane and some difficulties may be encountered for the following terms

$$Y_1 = \frac{\mathrm{H}_m^{(1)}(\lambda_0\omega)}{\mathrm{H}_m^{(1)\prime}(\lambda_0\omega)}, \quad Y_2 = \frac{\mathrm{J}_m(\lambda_1\omega)}{\mathrm{J}_m'(\lambda_1\omega)}, \quad Y_3 = \frac{\mathrm{Y}_m'(\lambda_1\omega h)\mathrm{J}_m(\lambda_1\omega) - \mathrm{J}_m'(\lambda_1\omega h)\mathrm{Y}_m(\lambda_1\omega)}{\mathrm{Y}_m'(\lambda_1\omega h)\mathrm{J}_m'(\lambda_1\omega) - \mathrm{J}_m'(\lambda_1\omega h)\mathrm{Y}_m'(\lambda_1\omega)}. \quad \text{(A 3)}$$

The derivatives of the Bessel, Neumann and Hankel functions are evaluated using the standard expression $X_m'(z) = [X_{m-1}(z) - X_{m+1}(z)]/2$ where X_m is either J_m, Y_m or $\mathrm{H}_m^{(1)}$.

The first problem concerns only Y_3 for which the cross-product of derivatives accumulates round-off error. If we use the relation $\mathrm{Y}_m = \mathrm{i}\mathrm{J}_m - \mathrm{i}\mathrm{H}_m^{(1)}$, we can rearrange the term Y_3 as follows

$$Y_3 = \frac{\mathrm{H}_m^{(1)\prime}(\lambda_1\omega h)\mathrm{J}_m(\lambda_1\omega) - \mathrm{J}_m'(\lambda_1\omega h)\mathrm{H}_m^{(1)}(\lambda_1\omega)}{\mathrm{H}_m^{(1)\prime}(\lambda_1\omega h)\mathrm{J}_m'(\lambda_1\omega) - \mathrm{J}_m'(\lambda_1\omega h)\mathrm{H}_m^{(1)\prime}(\lambda_1\omega)}.$$

It turns out that this expressions is less sensitive to round-off error and it can be traced back to the fact that the derivative of the Hankel function is never zero (it is always complex).

Another major issue is that for arguments z with large imaginary part, the Bessel functions behave like $\exp(|\mathrm{Im}(z)|)$ and the Hankel functions behave like $\exp(\mathrm{i}z)$. Thus, the magnitude of these functions is either very large or very small and these values may exceed the numerical accuracy. It is then necessary to use scaled functions: J_m is scaled by $\exp(-|\mathrm{Im}(z)|)$ and $\mathrm{H}_m^{(1)}$ by $\exp(-\mathrm{i}z)$. However, for very large arguments, we may still encounter problems due to round-off errors, especially for the denominator of Y_1, Y_2 and Y_3. It is then necessary to resort to asymptotic forms for large magnitude of $\lambda_0\omega$ and $\lambda_1\omega$:

$$Y_1 \simeq \frac{\mathrm{i} - 4\mathrm{i}m^2 - 8\lambda_0\omega}{3 + 4m^2 - 8\mathrm{i}\lambda_0\omega}, \quad Y_2 \simeq \mathrm{i}, \quad Y_3 \simeq \mathrm{i}.$$

A.3. *Inverse Fourier transform*

Evaluating the inverse Fourier transforms (3.20)–(3.23) is expensive since it requires the evaluation of the split function $\tilde{K}_+$ at a series of points distributed on the contour Γ. The number of points should be large to achieve a reasonable accuracy with standard quadrature schemes.

A way of reducing the number of points is to deform the contour Γ in a way similar to C so that $\tilde{K}_+$ is smooth on Γ. By doing so, it is possible to evaluate the split function on a reduced number of points. Then, the pressure and velocity potential for given coordinates (r, z) are computed using quadrature formulae to evaluate the integrals in (3.20)–(3.23). It should be noted that the values of the split function on the contour Γ have to be evaluated only once, the inverse transforms can then be computed for different sets of points.

The contour Γ is chosen to be similar to that described for the evaluation of split functions (see § A.1). However, the contours C and Γ should not overlap. Furthermore, we should note that the wavenumber u will have an imaginary part along Γ. If the quadrature scheme is inaccurate, the solution contains spurious terms $\exp(\mathrm{i}\omega uz)$ which are exponentially growing since the wavenumber u is complex. In theory, the contributions of these terms cancel each other, but they may remain if the integrals are not accurately evaluated.

REFERENCES

Alfredson, R. & Davies, P. 1970 The radiation of sound from an engine exhaust. *J. Sound Vib.* **13**, 389–408.

Aublin, B. 1996 Rayonnement et diffraction acoustique par un guide ouvert semi-infini. PhD thesis, Université de Technologie de Compigne, France.

Bento Coelho, J. 1980 Study of the characteristics of acoustic elements in flow ducts. MSc dissertation, University of Southampton, UK.

Bhattacharya, M. 1980 Engine noise source characterisation – an analysis and evaluation of experimental techniques. PhD thesis, University of Southampton, UK.

Cargill, A. 1982*a* Low frequency acoustic radiation from a jet pipe – a second order theory. *J. Sound Vib.* **83**, 339–354.

Cargill, A. 1982*b* The radiation of high frequency sound out of a jet pipe. *J. Sound Vib.* **83**, 313–337.

Carrier, G. 1956 Sound transmission from a tube with flow. *Q. Appl. Maths* **13**, 457–461.

Cho, Y. 1996 Exact solution for sound radiation from a circular duct with flows. In *Third Meeting of the Acoustical Society of America, Hawaii, December 1996*.

Crighton, D., Dowling, A., Ffowcs-Williams, J., Heckl, M. & Leppington, F. 1992 *Modern Methods in Analytical Acoustics*. Springer.

Crighton, D. & Leppington, F. 1974 Radiation properties of the semi-infinite vortex sheet: the initial-value problem. *J. Fluid Mech.* **64**, 393–414.

Free Field Technologies 2004 *Actran 2004 User's Manual*. Louvain-la-Neuve, Belgium.

Gabard, G., Astley, R. & Ben Tahar, M. 2005 Noise radiation from a jet pipe: a benchmark problem for computational aeroacoustics. In *11th AIAA/CEAS Aeroacoustics Conf*. *AIAA Paper* 2005–3064.

Goldstein, M. 1976 *Aeroacoustics*. McGraw–Hill.

Homicz, G. & Lordi, J. 1975 A note on the radiative directivity patterns of duct acoustic modes. *J. Sound Vib.* **41**, 283–290.

Jones, D. 1973*a* Instability due to acoustic radiation striking a vortex sheet on a supersonic stream. *Proc. R. Soc. Edin.* **71**, 121–140.

Jones, D. 1973*b* The reflection of an acoustic pulse by a plane vortex sheet. *Proc. Camb. Phil. Soc.* **74**, 347–362.

Jones, D. 1975*a* The effect of radiation due to a moving source on a vortex sheet. *Proc. R. Soc. Edin.* **72**, 195–205.

Jones, D. 1975*b* The scattering of sound by a vortex sheet. *J. Inst. Maths Applics.* **15**, 195–205.

Jones, D. 1977 The scattering of sound by a simple shear layer. *Phil. Trans. R. Soc. Lond.* **284**, 287–328.

Jones, D. & Morgan, J. 1972 The instability of a vortex sheet on a subsonic stream under acoustic radiation. *Proc. Camb. Phil. Soc.* **72**, 465–488.

Levine, H. & Schwinger, J. 1948 On the radiation of sound from an unflanged circular pipe. *Phys. Rev.* **73**, 383–406.

Morgan, J. 1974 The interaction of sound with a semi-infinite vortex sheet. *Q. J. Mech. Appl. Maths* **27**, 465–487.

Morgan, J. 1975 The interaction of sound with a subsonic cylindrical vortex sheet. *Proc. R. Soc. Lond.* A **344**, 341–362.

Munt, R. 1977 The interaction of sound with a subsonic jet issuing from a semi-infinite cylindrical pipe. *J. Fluid Mech.* **83**, 609–640.

Munt, R. 1990 Acoustic transmission properties of a jet pipe with subsonic jet flow. I. The cold jet reflection coefficient. *J. Sound Vib.* **142**, 413–436.

Noble, B. 1958 *Methods Based on the Wiener–Hopf Technique*. Pergamon.

Plumblee, H. & Dean, P. 1973 Sound measurements within and in the radiated field of an annular duct with flow. *J. Sound Vib.* **28**, 715–735.

Ramakrishnan, R. 1982 A note on the calculation of Wiener–Hopf split functions. *J. Sound Vib.* **81**, 592–595.

Rienstra, S. 1981 Sound diffraction at a trailing edge. *J. Fluid Mech.* **108**, 443–460.

Rienstra, S. 1983 A small Strouhal number analysis for acoustic wave–jet flow–pipe interaction. *J. Sound Vib.* **86**, 539–556.

Rienstra, S. 1984 Acoustic radiation from a semi-infinite annular duct in a uniform subsonic mean flow. *J. Sound Vib.* **94**, 267–288.

Schlinker, R. 1977 Transmission of acoustic plane-waves at a jet exhaust. In *AIAA Paper* 77-22.

Sutliff, D., Hall, D., Bridges, J. & Nallasamy, M. 1996*a* A unique ducted fan test bed for active noise control and aeroacoustics research. *NASA TM* 107213.

Sutliff, D., Nallasamy, M., Heidelberg, L. & Elliott, D. 1996*b* Baseline acoustic levels of the NASA active noise control fan rig. *NASA TM* 107214.

Taylor, M., Crighton, D. & Cargill, A. 1993 The low frequency aeroacoustics of buried nozzle systems. *J. Sound Vib.* **163**, 493–526.